


# c-Met-Targeting $^{19}\text{F}$ MRI Nanoparticles with Ultralong Tumor Retention for Precisely Detecting Small or Ill-Defined Colorectal Liver Metastases

Daoshuang Li<sup>1,2,\*</sup>, Jie Yang<sup>1,2,\*</sup>, Zuoyu Xu<sup>1,2</sup>, Yingbo Li<sup>1,2</sup>, Yige Sun<sup>1,2</sup>, Yuchen Wang<sup>1,2</sup>, Hongyan Zou<sup>1,2</sup>, Kai Wang<sup>1,2</sup>, Lili Yang<sup>1,2</sup>, Lina Wu<sup>1,2</sup>, Xilin Sun<sup>1,2</sup> 

<sup>1</sup>Department of Nuclear Medicine, the Fourth Hospital of Harbin Medical University, Harbin, Heilongjiang, People's Republic of China; <sup>2</sup>NHC Key Laboratory of Molecular Probe and Targeted Diagnosis and Therapy, Molecular Imaging Research Center (MIRC) of Harbin Medical University, Harbin, Heilongjiang, People's Republic of China

\*These authors contributed equally to this work

Correspondence: Xilin Sun; Lina Wu, Department of Nuclear Medicine, the Fourth Hospital of Harbin Medical University, 766 Xiangnan N Street, Songbei District, Harbin, Heilongjiang, 150028, People's Republic of China, Tel +86-451-88118600, Fax +86-451-82576509, Email sunxl@ems.hrbmu.edu.cn; LinaWu@hrbmu.edu.cn

**Purpose:** Precisely detecting colorectal liver metastases (CLMs), the leading cause of colorectal cancer-associated mortality, is extremely important.  $^1\text{H}$  MRI with high soft tissue resolution plays a key role in the diagnosing liver lesions; however, precise detecting CLMs by  $^1\text{H}$  MRI is a great challenge due to the limited sensitivity. Even though contrast agents may improve the sensitivity, due to their short half-life, repeated injections are required to monitor the changes of CLMs. Herein, we synthesized c-Met-targeting peptide-functionalized perfluoro-15-crown-5-ether nanoparticles (AH111972-PFCE NPs), for highly sensitive and early diagnosis of small CLMs.

**Methods:** The size, morphology and optimal properties of the AH111972-PFCE NPs were characterized. c-Met specificity of the AH111972-PFCE NPs was validated by in vitro experiment and in vivo  $^{19}\text{F}$  MRI study in the subcutaneous tumor murine model. The molecular imaging practicability and long tumor retention of the AH111972-PFCE NPs were evaluated in the liver metastases mouse model. The biocompatibility of the AH111972-PFCE NPs was assessed by toxicity study.

**Results:** AH111972-PFCE NPs with regular shape have particle size of  $89.3 \pm 17.8$  nm. The AH111972-PFCE NPs exhibit high specificity, strong c-Met-targeting ability, and precise detection capability of CLMs, especially small or ill-defined fused metastases in  $^1\text{H}$  MRI. Moreover, AH111972-PFCE NPs could be ultralong retained in metastatic liver tumors for at least 7 days, which is conducive to the implementation of continuous therapeutic efficacy monitoring. The NPs with minimal side effects and good biocompatibility are cleared mainly via the spleen and liver.

**Conclusion:** The c-Met targeting and ultralong tumor retention of AH111972-PFCE NPs will contribute to increasing therapeutic agent accumulation in metastatic sites, laying a foundation for CLMs diagnosis and further c-Met targeted treatment integration. This work provides a promising nanopatform for the future clinical application to patients with CLMs.

**Keywords:** c-Met-targeted, perfluorocarbon,  $^{19}\text{F}$  MRI, colorectal liver metastases, precise detection

## Introduction

The liver is the most common dominant metastatic site for colorectal cancer (CRC), with approximately 50% of patients with CRC developing in their lifetime liver metastases, the leading cause of CRC-associated mortality.<sup>1,2</sup> Precise imaging of colorectal liver metastases (CLMs) is critical for treatment ensuing in prolonged survival.<sup>3-5</sup> Over-expression of the c-mesenchymal-epithelial transition factor (c-Met) gene has been proposed as a prognostic factor, contributing to the malignant transformation of colonic epithelial cells and the development of CLMs.<sup>6-8</sup> In addition, recent studies have shown an attractive antitumor activity of c-Met targeted drugs in CRC and CLMs.<sup>9-12</sup> Therefore, it is of great

significance to take c-Met as the target for precise imaging diagnosis and monitoring the targeted therapy to patients with CLMs.

Magnetic resonance imaging (MRI) does not use radionuclides or ionizing radiation and is considered one of the most promising imaging techniques. As living tissues contain 65–80% of mobile water, different relaxation properties of hydrogen atoms have been exploited by clinical  $^1\text{H}$  MRI to provide precise anatomical information with high soft tissue resolution.<sup>13,14</sup> The high water content also nevertheless results in strong background, leading to reduced contrast and limited sensitivity of  $^1\text{H}$  MRI for detection of CLMs.<sup>15–17</sup> Although clinically used contrast agents (CAs) such as gadolinium (Gd) chelates may facilitate the detection of liver lesions, the lack of tumor targeting ability compromise their accuracy in tumor diagnosis. Furthermore, because of their short half-life, repeated injections are required to monitoring tumor changes, which leads to an increased risk of nephrogenic systemic fibrosis (NSF).

Surrogate nuclei-based MRI is a fundamental approach to the background issue.  $^{19}\text{F}$  with high magnetic resonance sensitivity and 100% natural abundance seems to be the most promising candidate among these nuclei.<sup>18</sup> More significantly, endogenous  $^{19}\text{F}$  nuclei are mainly present in teeth and bones in solid form.<sup>19</sup> Therefore,  $^{19}\text{F}$  MRI with the introduction of exogenous fluorine nuclei is considered to be a zero-background imaging modality with high tissue penetration depth. The accuracy and sensitivity of  $^{19}\text{F}$  MRI are greatly improved with the advancement of the dual  $^1\text{H}/^{19}\text{F}$  radiofrequency (RF) coil. Perfluorocarbons (PFCs), such as perfluoro-15-crown-5-ether (PFCE), with strong stability, non-toxicity, and high fluorine density, can improve the detection sensitivity of  $^{19}\text{F}$  MRI and have been extensively used as  $^{19}\text{F}$  MRI agents.<sup>20,21</sup> Furthermore, PFCs tend to have long biological retention, suited for long-term monitoring of intrahepatic lesion changes with only one single injection.<sup>22</sup> Although PFCs have been demonstrated to have enormous potential for applications in  $^{19}\text{F}$  MR molecular imaging, including for cell tracking and sensing of oxygen partial pressure, c-Met-targeting PFC-based NPs have not been successfully developed and applied for the detection of CLMs until now.

In this study, for the first time, we synthesized and employed c-Met-targeting peptide-functionalized perfluoro-15-crown-5-ether nanoparticles, AH111972-PFCE NPs, for  $^{19}\text{F}$  MRI of CLMs (Scheme 1). The current analysis aimed to assess c-Met specific targeting,  $^{19}\text{F}$  MR imaging feasibility, and prolonged tumor retention of AH111972-PFCE NPs for accurate detection of CLMs.

## Materials and Methods

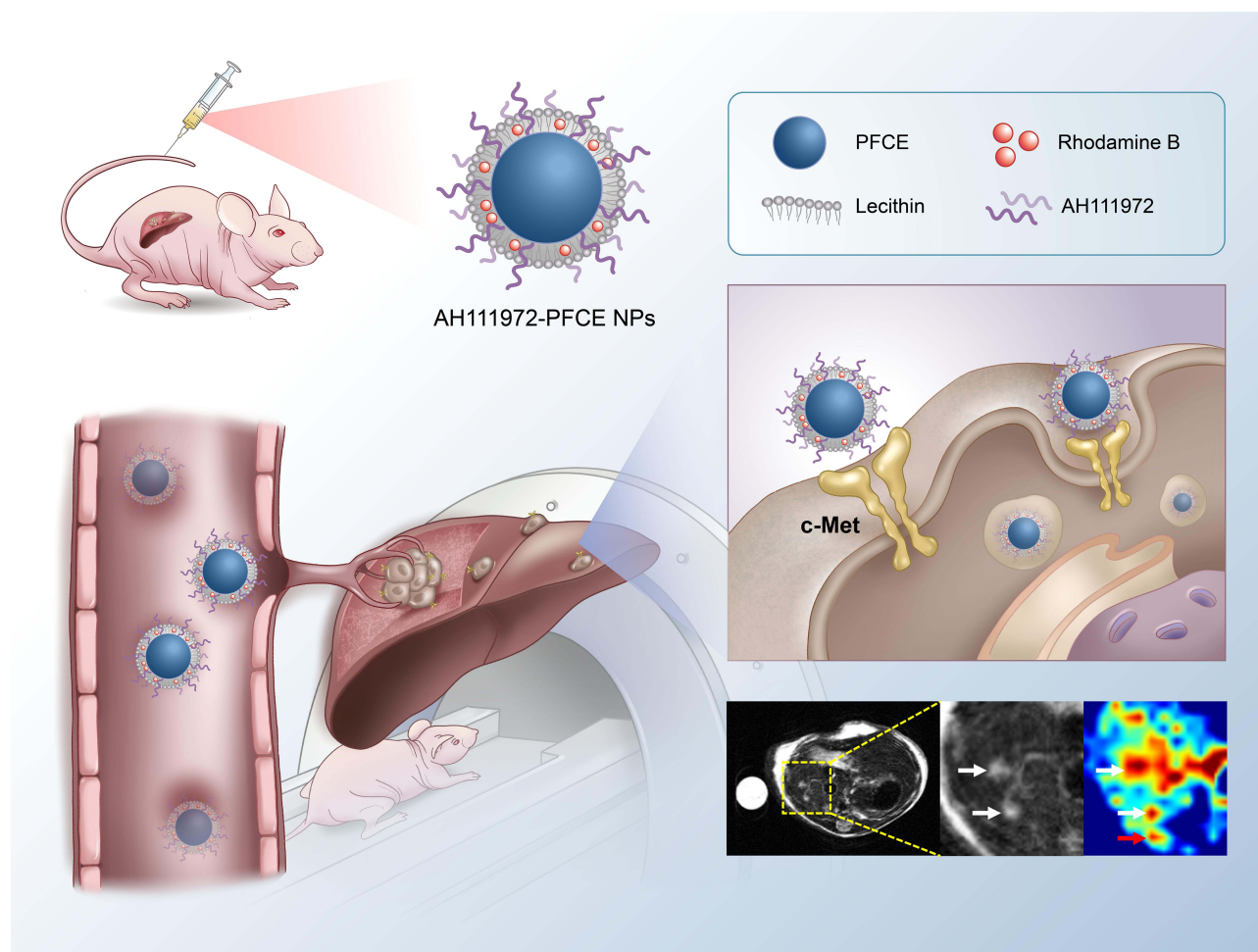
### Cell Lines and Reagents

The human CRC cell lines, Lovo and SW948, purchased from Procell Life Science & Technology Co., Ltd. (HB, CHN) were grown cultured in F-12K and Leibovitz's L-15 medium, respectively, supplemented with 10% fetal bovine serum (FBS) and 1% penicillin-streptomycin (Gibco, Invitrogen Life Technology, Carlsbad, CA, USA). Cells were maintained at 37°C in a humidified atmosphere.

Perfluoro-15-crown-5-ether (PFCE) was obtained from Exfluor Research Corporation (TX, USA). Cholesterol, 2-dipalmitoyl-sn-glycero-3-phosphoethanolamine-N-(lissaminerhodamine B sulfonyl) (16:0 Liss Rhod PE) and high-purity lecithin were bought from Avanti Polar Lipids, Inc. (AL, USA). AH111972 cyclic peptide (Cys4-16, 6-14; Ac-Ala-Gly-Ser-Cys-Tyr-Cys-Ser-Gly-Pro-Pro-Arg-Phe-Glu-Cys-Trp-Cys-Tyr-Glu-Thr-Glu-Gly-Thr-Gly-Gly-Gly-Lys) was purchased from China Peptide Co., Ltd. (HB, CHN). Glycerin was provided by Aldrich Chemical Co. (WI, USA). Argon (Ultra High Purity: UHP, 99.99%) was used to store materials. The Spectra/Por membrane (Cellulose MWCO: 20kDa) used for dialysis was procured from Spectrum Medical Industries, Inc. (CA, USA).

### Preparation of AH111972-PFCE NPs

c-Met-targeting and non-targeting PFCE nanoparticles were formulated, as previously described.<sup>23</sup> Briefly, the nanoparticles consist of 20% (v/v) PFCE, 2.5% (w/v) glycerin, 2% (w/v) of a surfactant commixture, and water representing the balance. The surfactant were comprised of 85 mol % lecithin, 12 mol % cholesterol, 2.9 mol % dipalmitoyl phosphatidylglycerol (DPPG) and 0.1 mol % 1,2-dipalmitoyl-sn-glycerol-3-phosphoethanolamine-N-(lissaminerhodamine B sulfonyl) (16:0 Liss Rhod PE). The lipids were solubilized in a mixture of methanol and chloroform, filtered through



**Scheme 1** Schematic illustration of targeted binding of AH111972-PFCE NPs to c-Met for precise detection of missing and ill-defined colorectal liver metastases.

a small cotton bed, and dried into thin film by rotary evaporation at 45°C under reduced pressure, and then further dried in a vacuum oven (45 °C) for 24 hours. Subsequently, the lipid film was hydrated with purified water, vortexed at high speed for 2 mins and the probe was sonicated for 2 mins. The M110P Microfluidics emulsifier (Microfluidics, Newton, MA) was used to emulsify the nanoparticles and AH111972 (10.0 mg) was dissolved in pre-emulsion (1.0 mL) solution. Then use a 20 kDa MWCO cellulosic membrane to dialyzed against the deionized water of the products. The completed c-Met-targeting nanoparticles were placed in aseptically sealed vials, blanketed with argon, and stored in the refrigerator (4 °C) overnight prior to further use. The nontargeted PFCE NPs were prepared similarly but without AH111972.

## Characterization of Nanoparticles

The hydrodynamic diameter, stability, and zeta potential ( $\zeta$ ) of the c-Met-targeting PFC NPs were analyzed by dynamic light scattering (DLS) on a Malvern Nano ZS Zetasizer (Malvern Instruments Ltd, Malvern, UK). All assays were carried out in multiples of three consecutive measurements. The morphology of nanoparticles was detected under a transmission electron microscope (TEM, Talos F200s, acceleration voltage = 200 kV). Elemental mapping images were also obtained by using transmission electron microscope. The absorption spectra of the c-Met-targeting PFC NPs were analyzed by ultraviolet and visible spectrophotometry (UV-vis) on a Lambda35 spectrophotometer (PerkinElmer, USA).

PFCE content of AH111972-PFCE NPs was measured with a 9.4 T NMR spectrometer (Bruker Avance III 400 MHz), equipped with a BBFO-probe. AH111972-PFCE NPs were dissolved in D<sub>2</sub>O (Sigma Aldrich, GER) and CF<sub>3</sub>COONa (Sigma Aldrich, GER) was added as an internal reference. The mixture was measured at -75.4 ppm with a 50 ppm

spectral width, take the average of 8 measurements with an interscan delay of 25 seconds. Data were analyzed with Topspin 4.1.3.

## Measurement of AH11972 Content in AH11972-PFCE NPs

To detect the AH11972 content in AH11972-PFCE NPs, ultraviolet and visible spectrophotometry (UV-vis) was used. Briefly, the absorbance spectra of the AH11972-PFCE NPs were obtained on a UV-vis spectrometer (Lambda35, PerkinElmer, USA). The AH11972 standard solutions were prepared at concentrations ranging from 0.8 to 10 mg / mL. The working curve was obtained based on the absorbance of the peak at about 275 nm. Finally, the AH11972 content of the AH11972-PFCE NPs could be calculated according to the working curve shown in [Figure S2](#).

## Phantom Experiments

AH11972-PFCE NPs were dissolved in 1.7% agarose solution at concentrations of 4.6, 6.9, 9.2, 13.8, 18.4, and 27.6 mM and transferred to tubes.  $^{19}\text{F}$  phantom images were captured on a 9.4T small animal MR scanner (BioSpec 94/20 USR, Bruker, Germany) using a rapid acquisition with relaxation enhancement (RARE) sequence, the parameters were as follows: echo times (TE) = 100msec; repetition time (TR) = 2000 msec; matrix = 64×64; field of view (FOV) = 38.4×38.4 mm; slice thickness = 1 mm.

## Animal Models

Female BALB/c nude mice, 6-8-week-old, were obtained from Vital River Laboratory Animal Technology Co., Ltd. (BJ, CHN) and raised under specific pathogen-free conditions with free access to food and water. All animal experiments in this study were approved by the Medical Ethics Committee of the Fourth Hospital of Harbin Medical University and complied with Laboratory Animal-Guideline for Ethical Review of Animal Welfare (GB/T 35892-2018). For the mouse model with liver metastases, mice were anesthetized with isoflurane and placed in the right lateral decubitus position. A small longitudinal incision was made in the left upper abdomen of the mouse. Expose the spleen with a small retractor.  $1 \times 10^6$  SW948 cells were inoculated in a 50  $\mu\text{L}$  volume of PBS and then injected into the lower pole of the spleen parenchyma. After returning the spleen to the abdominal cavity, the subcostal incision was stitched up with a 5–0 absorbable suture. For the subcutaneous CRC murine model, each mouse was injected subcutaneously with  $2 \times 10^6$  SW948 cells suspended in 100  $\mu\text{L}$  of PBS on the right side of the back.

## Western Blot Analysis

Total protein samples were collected from SW948 and Lovo cells in RIPA lysis buffer containing protease inhibitors at an ice-cold bath. The resulting lysates were centrifugated at  $12.3 \times 10^3$  rpm at 4 °C for 5 min and the supernatant was gathered. The extracted total proteins were measured using the BCA protein assay kit (Bio-Rad Protein Assay) according to the manufacturer's instruction. Corresponding samples with equal amounts of protein were separated by SDS-PAGE and proteins were transferred to polyvinylidene fluoride (PVDF) membrane and blocked with 5% milk. After washing with PBS, the PVDF membrane was incubated with c-Met primary antibodies (Cell Signaling Technology, USA) overnight at 4°C. The blots were washed with TBST buffer and incubated with the goat anti-rabbit IgG HRP-linked secondary antibody for 2 hours at room temperature. Chemiluminescent signals were detected by the ChemiDoc XRS system (Bio-Rad) using GAPDH as a loading control.

## Fluorescence Microscopy

For in vitro fluorescence microscopy,  $1 \times 10^5$  cells were seeded in a 35-mm-diameter glass-bottom petri dish and grown under 5%  $\text{CO}_2$  at 37°C for 48 hours, then washed 3 times with PBS and fixed with 4% paraformaldehyde for 15 minutes. Cells were subsequently incubated with rabbit anti-c-Met monoclonal antibody (Cell Signaling Technology, 8198) at 4°C overnight. Cells were then incubated with the Alexa Fluor 488-labeled polyclonal goat anti-rabbit IgG as secondary fluorescence antibody for 1 hour at room temperature. Cells were again washed 3 times, and the nuclei were stained with 4',6-diamidino-2-phenylindole (DAPI) for 5 minutes. Fluorescence microscopy was performed with a confocal laser scanning microscope (Nikon C2plus, Japan).



## Cell Uptake

Cells were seeded in a 35-mm-diameter glass-bottom Petri dish at a density of  $5 \times 10^4$  cells/mL. After 24 hours of incubation, the growth medium was replaced with AH111972-PFCE NPs or non-targeted PFCE NPs (40  $\mu$ L /mL culture media) and cells were incubated at 37°C for 4 hours. Cells in the blocking group were pre-incubated with excess free AH111972 for 3 hours before incubating with AH111972-PFCE NPs. Thereafter, cells were washed with PBS and fixed in 4% paraformaldehyde (PFA). After washing with PBS for 3 times, the nuclei were stained with DAPI. Finally, each dish was washed three times and cells were analyzed using a Nikon C2 plus confocal laser scanning microscope (Nikon, Japan).

## Cell Viability

Colorimetric 3-(4,5-dimethylthiazol-2-yl)-2,5-diphenyltetrazolium bromide (MTT) assay was used to evaluate cell viability. Cells were seeded in a 96-well plate at a concentration of  $1 \times 10^4$  cells/well, and incubated for 24 hours. Then the cells were exposed to different concentrations (4.6, 6.9, 9.2, 13.8, 18.4, and 27.6 mM) of AH111972-PFCE NPs, in a final volume of 200  $\mu$ L per well. After 24 hours of incubation, each well was added with 20  $\mu$ L MTT solution (5 mg/mL) according to the manufacturer's instructions, then the plates were incubated for additional 4 hours at 37°C. Then, the culture medium in each well was removed completely and replaced with 150  $\mu$ L dimethyl sulfoxide (DMSO), and the absorbance of each well at 490 nm was recorded on a computer-controlled plate-reader (Biotech, USA).

## Cell Apoptosis

Cells were cultured in a 35-mm-diameter glass-bottom Petri dish and treated with AH111972-PFCE NPs for 24 hours at a concentration of 27.6 mM in a final volume of 1 mL. Then cells were washed with PBS and fixed with 4% PFA for 30 minutes. Subsequently, the terminal deoxynucleotidyl-transferase-mediated dUTP-biotin nick-end labeling (TUNEL) assay was conducted using the in situ Cell Death Detection Kit in the light of the manufacturer's instructions (Roche). Finally, samples were stained with DAPI to visualize cell nuclei and examined under fluorescence microscopy (Nikon, Japan).

## MRI Scan

Prior to the MRI scan, mice were anesthetized by inhalation of isoflurane gas, the respiration rates of mouse were monitored during MRI scan. The temperature of each mouse was controlled at  $37.0 \pm 0.2$  °C throughout MRI scan by using an automated temperature control system (Thermo Fisher Scientific).

MRI data of subcutaneous SW948 tumor mice were recorded on a 9.4T small animal MR scanner (Bruker, Germany) equipped with a  $^1\text{H}/^{19}\text{F}$  dual-tuned volume coil. Mouse in the nonblocking group were administered AH111972-PFCE NPs or non-targeting PFCE NPs (300  $\mu$ L / mouse) with a PFCE concentration of 18.4 mM through the tail vein. For each mouse in the blocking group, 3 mg free AH111972 was administrated intravenously via the tail vein 3 hours prior to the injection of AH111972-PFCE NPs.  $^1\text{H}$  ( $T_1$ -weighted) and  $^{19}\text{F}$  images were acquired before injection and at different time points after the injection. The MRI results of SW948 liver metastases model were also collected on a 9.4T small animal MR scanner equipped with a  $^1\text{H}/^{19}\text{F}$  dual-tuned volume coil.  $^1\text{H}$  ( $T_2$ -weighted) and  $^{19}\text{F}$  images of mice in the AH111972-PFCE NPs group (100  $\mu$ L / mouse) and the non-targeted PFCE NPs group (100  $\mu$ L / mouse) as well as  $^1\text{H}$  ( $T_1$ -weighted) images of mice in the gadoterate meglumine (Gd-DOTA) group (4  $\mu$ L / mouse) were collected before and after intravenous injection via the tail vein.  $^1\text{H}$  images were acquired using RARE sequence, and scan parameters for  $T_1$  RARE sequence were set as follows: repetition time (TR) = 820 msec, time to echo (TE) = 12 msec, number of averages (NA) = 2, RARE factor = 8, matrix size =  $256 \times 256$ , field of view (FOV) =  $38.4 \times 38.4$  mm<sup>2</sup>, slice thickness = 1.0 mm; scan parameters for  $T_2$  RARE sequence were set as follows: TR = 3000 msec, TE = 40 msec, NA = 2, RARE factor = 10, matrix size =  $256 \times 256$ , FOV =  $38.4 \times 38.4$  mm<sup>2</sup>, slice thickness = 1.0 mm. The  $^{19}\text{F}$  image colocalized with proton image was done with a RARE sequence, imaging parameters: TR = 2000 msec, TE = 100 msec, NA = 128; RARE factor = 32, matrix size =  $64 \times 64$ , FOV =  $38.4 \times 38.4$  mm<sup>2</sup>, slice thickness = 3.0 mm. An Eppendorf (EP) tube containing AH111972-PFCE NPs dissolved in 1.7% agarose solution was applied as an internal reference. Following the final time point, the mice were sacrificed and organs were collected for ex vivo imaging experiment.

The PFCE concentration of tumor was calculated: (PFCE concentration of reference tube containing 17.88 mM of AH111972-PFCE NPs  $\times$   $^{19}\text{F}$  signal intensity of tumor /  $^{19}\text{F}$  signal intensity of the reference tube in the same plane). Data analysis of  $^{19}\text{F}$  signal intensity was performed using the workstation (Para Vision Acquisition 6.0.1) software.

## Ex vivo Biodistribution

Mice were injected with AH111972-PFCE NPs for 72 hours and euthanized. Tumor tissues and major organs including brain, heart, intestine, liver, kidney, spleen, and lung were excised for ex vivo biodistribution studies. Images were captured using a IVIS spectrum imaging system (Xenogen, USA) with the following parameters: excitation 535 nm, emission DsRed, exposure time 1s, binning factor 2, F number 4, FOV 12.5.

## Ex vivo Immunofluorescence

Mice with subcutaneous SW948 tumors were sacrificed 72 hours after injecting with AH111972-PFCE NPs. The tumor tissues were frozen in optimal cutting temperature compound (OCT) and cryo-sectioned at 5  $\mu\text{m}$  thickness with a microtome (LEICA CM3050S, Solms, Germany). The tumor sections were directly stained with DAPI for 5 minutes. Images were acquired with a C2 plus (Nikon, Japan) confocal laser scanning microscope.

## Toxicity Study

A toxicity study was tested following intravenous injection with 100  $\mu\text{L}$  of AH111972-PFCE NPs to 7-week-old healthy female BALB/c nude mice; saline was injected into mice in the control group. Terminal blood was gathered by cardiac puncture 1 day and 30 days after the injection and the serum was transferred immediately to a microcentrifuge tube. Subsequently, indicators of renal and hepatic function including creatinine (Crea), blood urea nitrogen (BUN), serum aspartate aminotransferase (AST) and alanine aminotransferase (ALT) were measured. Additionally, white blood cells (WBC), red blood cells (RBC) and platelets (PLT) were counted for the routine blood test. Tissues including the heart, liver, kidney, spleen and lung of mouse 30 days post injection were quickly removed and immediately fixed in 4% paraformaldehyde. Then the tissues were dehydrated in a graded series of alcohol, and sampled for paraffin-embedding. Hematoxylin and eosin (H&E) staining were performed after the preparation of tissue slices (5  $\mu\text{m}$ ). All sections were observed under an IX71 (Olympus, Tokyo, Japan) research microscope.

## Statistical Analysis

Statistical analysis was performed using the Prism 8 Software (GraphPad Software, La Jolla, CA). All data were expressed as the mean  $\pm$  standard deviation. Analyses of differences between groups were performed using Student's *t*-test. The difference among groups was assessed by analysis of variance (ANOVA). Error bars indicate the standard error of the mean (SEM) unless otherwise stated. We considered *P* values  $< 0.05$  to indicate a statistically significant difference.

## Results

### Characterization of AH111972-PFCE NPs

The transmission electron microscopy (TEM) images demonstrated that AH111972-PFCE NPs have regular shape morphology and the size was  $89.3 \pm 17.8$  nm (Figure 1a and b). Zeta potentials of AH111972-PFCE NPs and non-targeted PFCE NPs were  $-31.30 \pm 1.74$  mV and  $-4.09 \pm 0.83$  mV, respectively (Figure 1c). Dynamic laser scattering (DLS) result confirmed the size and the hydrodynamic behavior of non-targeted PFCE and AH111972-PFCE NPs (Figure 1d and e). No obvious changes in the size of AH111972-PFCE NPs were observed after the incubation in water and 10% FBS for 10 days, and the zeta potential did not change significantly during this period (Figures 1f, g and S1, Supporting Information). The existence of elements C, O, N, F and S in AH111972-PFCE NPs was further demonstrated by elemental mapping images (Figure 1h). As shown in Figure 1i, the ultraviolet (UV) absorption curve of AH111972-PFCE NPs represented the characteristic peak of AH111972 at 275 nm, confirming AH111972 binding to PFCE NPs.

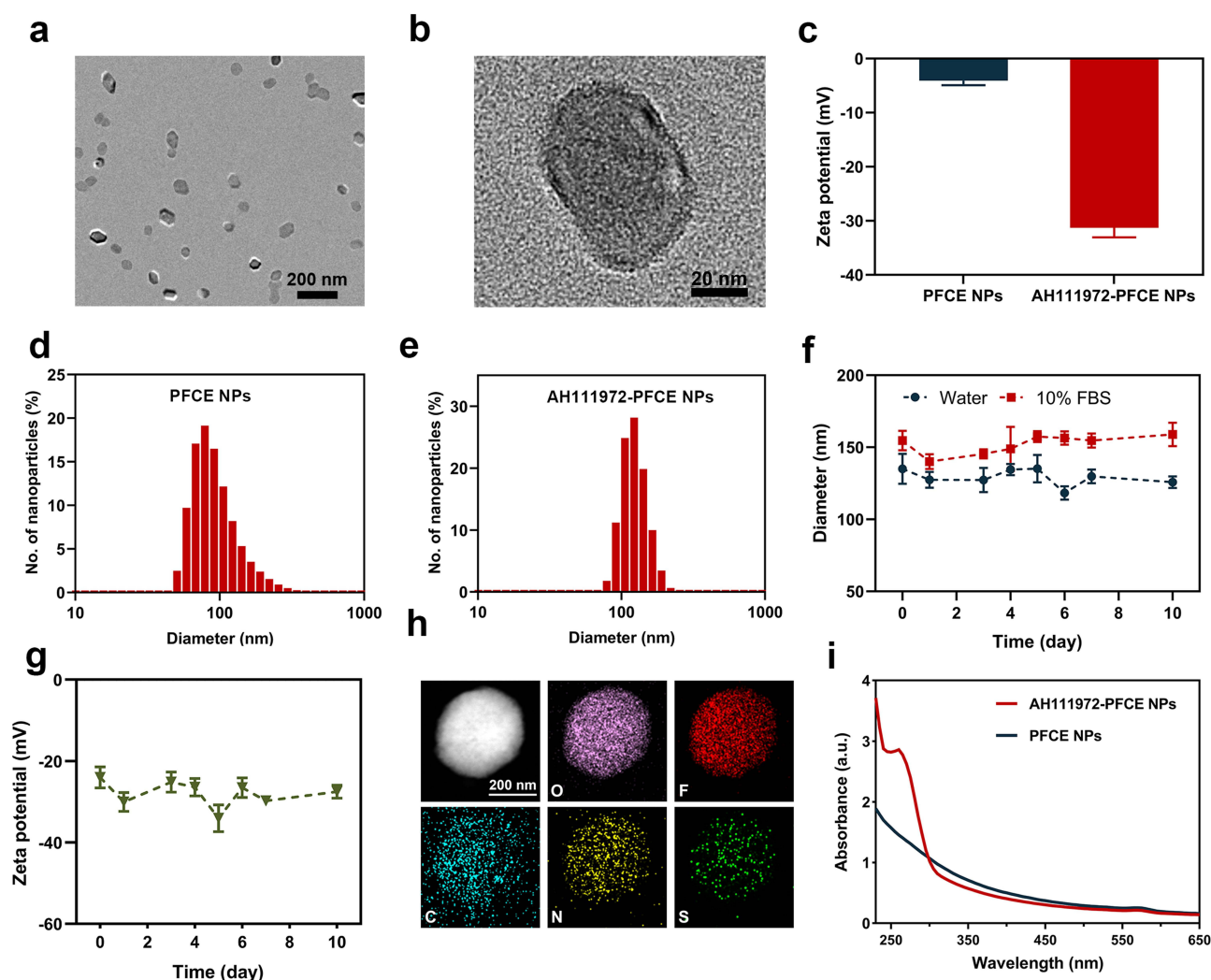


**Figure 1** Characteristics of AH111972-PFCE NPs. (a and b) The TEM image of AH111972- PFCE NPs. (c) Zeta potential of AH111972-PFCE and non-targeted PFCE NPs. (d) DLS measurement of PFCE NPs. (e) DLS measurement of AH111972-PFCE NPs. (f) The hydrodynamic size of AH111972-PFCE NPs dispersed in water and 10% FBS over 10 days. (g) Zeta potential of AH111972-PFCE NPs over 10 days. (h) High-angle annular dark field (HAADF) image as well as nitrogen (N), fluorine (F), oxygen (O), carbon (C) and sulfur (S) elemental mapping of AH111972-PFCE NPs; Scale bar is 200 nm. (i) UV absorption spectra of AH111972-PFCE NPs and PFCE NPs.

The characteristic peak of rhodamine B at 570 nm was present in AH111972-PFCE NPs and non-targeted PFCE NPs. The standard curve of AH111972 was displayed in [Figure S2, Supporting Information](#).

The MRI of phantoms with AH111972-PFCE NPs showed a highly linear ( $R^2 = 0.9971$ ) correlation of signal-to-noise ratio (SNR) at a range of concentrations from 4.6 to 27.6 mmol/L ([Figure 2a and b](#)). This linear relationship between the phantom concentration and SNR indicated that the  $^{19}\text{F}$  MRI signal intensity was dependent only on the concentration of PFCE, which is beneficial for the quantification in vivo. Also, a single resonance peak indicated that the PFCE-based NPs possessed optimal characteristics for imaging ([Figure 2c](#)).

## In vitro Cellular Uptake Study

SW948 and Lovo cells were chosen as CRC cell models for the cellular uptake study, and c-Met-overexpression was validated by Western blotting and fluorescence microscopy. c-Met expression of SW948 cells detected by Western blotting was significantly higher than that of Lovo cells ([Figure 3a and b](#)). The results were also supported by fluorescence microscopy ([Figure 3c and d](#)). Subsequently, in vitro cellular uptake study was conducted on both cell models. After 4 h of incubation with AH111972PFCE NPs or non-targeted PFCE NPs, cells were assessed for nanoparticle uptake using confocal laser scanning microscopy (CLSM). Significantly higher uptake of AH111972-

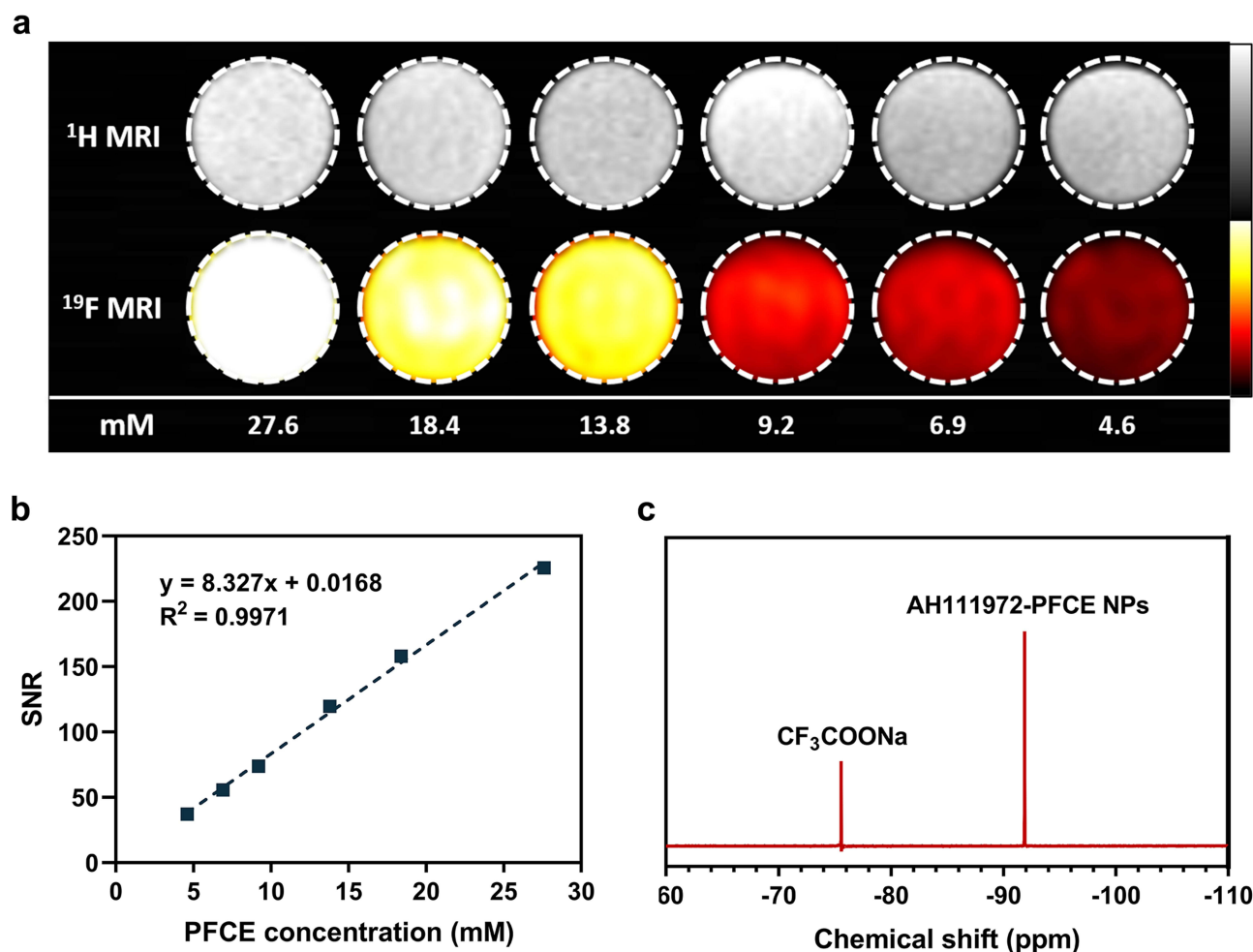


**Figure 2** MRI characterization of AH111972-PFCE NPs. (a)  $^{19}\text{F}$  MRI of a dilution series of AH111972-PFCE NPs dissolved in 1.7% agarose solution. (b) Plot of the  $^{19}\text{F}$  MRI signal-to-noise ratio (SNR) versus PFCE concentration. (c)  $^{19}\text{F}$  NMR spectrum showing the AH111972-PFCE NPs singlet in relation to an internal sodium trifluoroacetate ( $\text{CF}_3\text{COONa}$ ) reference standard.

PFCE NPs than non-targeting PFCE NPs in SW948 cells was confirmed by CLSM images with substantially enhanced fluorescence intensity detected through the rhodamine B channel in red color. Furthermore, cells pre-incubated with free AH111972 in the blocking group showed dramatically reduced uptake of AH111972-PFCE NPs (Figure 3e and f). However, incubation of AH111972-PFCE NPs in the absence or presence of free AH111972 and incubation with non-targeting PFCE NPs had no apparent effect on the uptake by Lovo cells (Figure S3, Supporting Information).

## Validation of c-Met Specificity of AH111972-PFCE NPs in the Subcutaneous SW948 Tumor Model

The effectiveness of AH111972-PFCE NPs as the  $^{19}\text{F}$  MR molecular imaging probe to specifically detect disease in vivo was verified using a subcutaneous SW948 tumor murine model. As shown in Figure 4a, the  $^{19}\text{F}$  MR signals could be detected in the tumor boundary at 1 h post injection of AH111972-PFCE NPs that progressively penetrated into the whole tumor. However, the tumor  $^{19}\text{F}$  MR signal intensity was negligible at all time points in mice receiving non-targeting PFCE NP injection. The in vivo c-Met-targeting capability of AH111972-PFCE NPs was further confirmed in the receptor blocking experiment. MRI images of mice receiving pre-injection of AH111972 blocking reagent exhibited almost no uptake of AH111972-PFCE NPs in the tumor. Quantitative analysis of the imaging data revealed that the PFCE concentrations in tumor regions of the AH111972-PFCE NP group were markedly higher than that of other groups at 4 h post-injection. Moreover, the PFCE concentration of tumor in the AH111972-PFCE NP group continued to increase



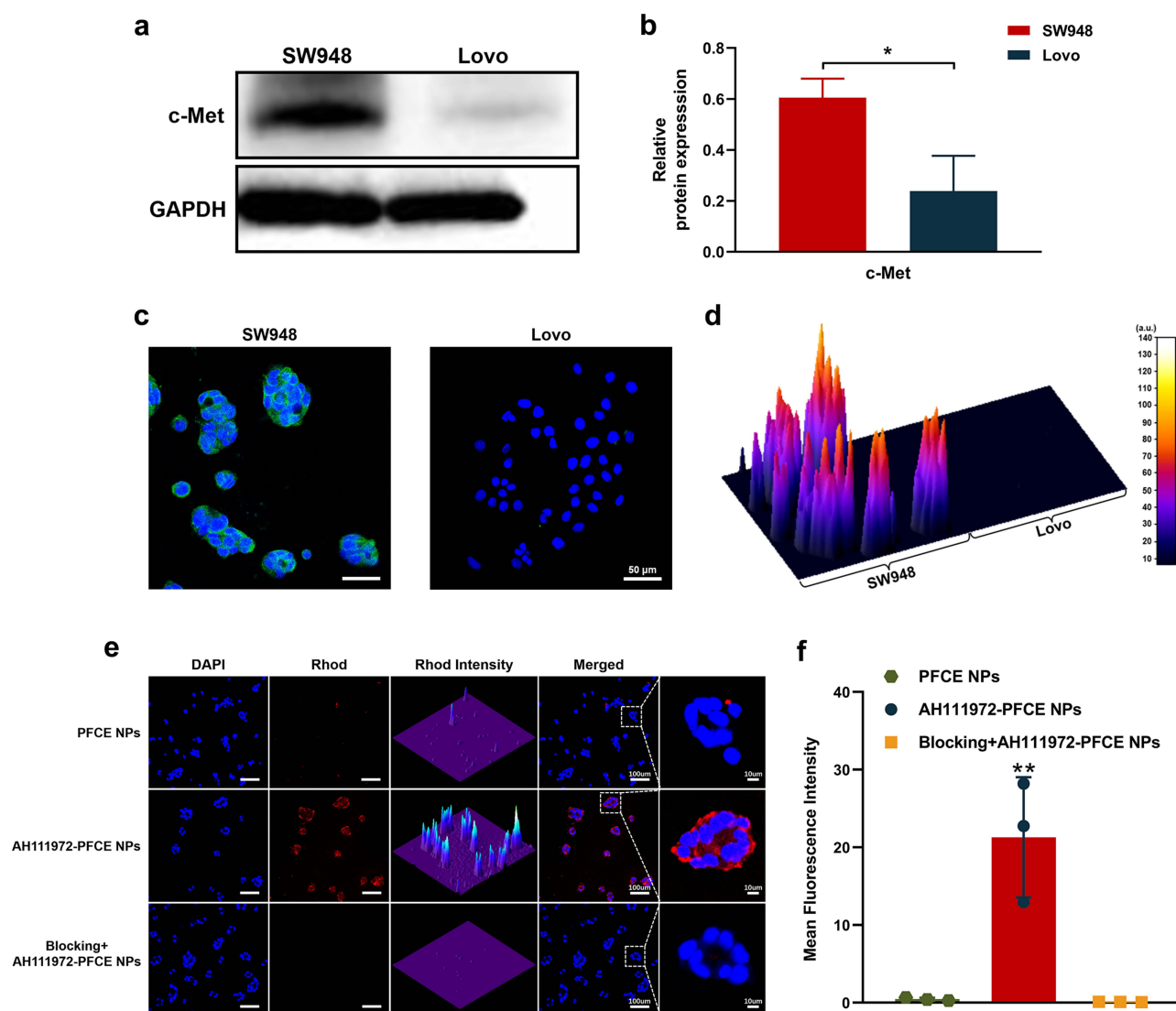


**Figure 3** Cell uptake of AH111972-PFCE NPs in vitro. (a) c-Met expression of SW948 and Lovo cells analyzed by Western blot. (b) Quantitative analysis of relative protein expression in SW948 and Lovo cells. (c) Confocal laser scanning microscopy images and (d) surface plot of c-Met in SW948 and Lovo cells; Scale bar is 50  $\mu$ m. (e) Cell uptake efficiency of SW948 cells to AH111972-PFCE NPs and PFCE NPs detected by confocal laser scanning microscopy; Scale bar is 100  $\mu$ m. Cells in blocking group were pre-incubated with free AH111972 for 3 h followed by incubation with AH111972-PFCE NPs. (f) Quantitative analysis of mean fluorescence intensity in SW948 cells in each group. Data were expressed as mean  $\pm$  SD, \* $P$  < 0.05, \*\* $P$  < 0.01.

significantly compared with non-targeting PFCE NP group and blocking group, the mean value was  $16.05 \pm 2.54$ ,  $2.53 \pm 0.80$ ,  $1.49 \pm 0.48$  mM, respectively, at final time point (Figure 4b). Ex vivo biodistribution studies validated the  $^{19}\text{F}$  MRI results. Besides the liver and spleen, established sites of PFC deposition,<sup>22</sup> the accumulation of fluorescent NPs was only detected in tumors from mice injected with AH111972-PFCE NPs (Figure 4c and d). Immunofluorescence staining revealed that mice in the non-targeting PFCE NPs and the blocking groups showed insignificant uptake of fluorescent NPs in the tumor. In contradistinction, microscopy of the subcutaneous tumor tissue 72 h after injection with AH111972-PFCE NPs showed permeation of the NPs into the tumor (Figure 4e and f).

The robust tumor-targeting capability of the AH111972-PFCE NPs could be attributed to several factors. First, the 26-amino acid cyclic peptide AH111972 has a high affinity for c-Met. Second, the size of the AH111972-PFCE NPs contributes to increasing the ligand-receptor interaction per particle. Third, the NPs have long-term circulation allowing for increased tumor-targeting capability.<sup>24,25</sup> Finally, the negative surface charge of AH111972-PFCE NPs increases their stability in the serum-free culture medium and subsequently their affinity for the cell membrane.<sup>26</sup> Moreover, AH111972-

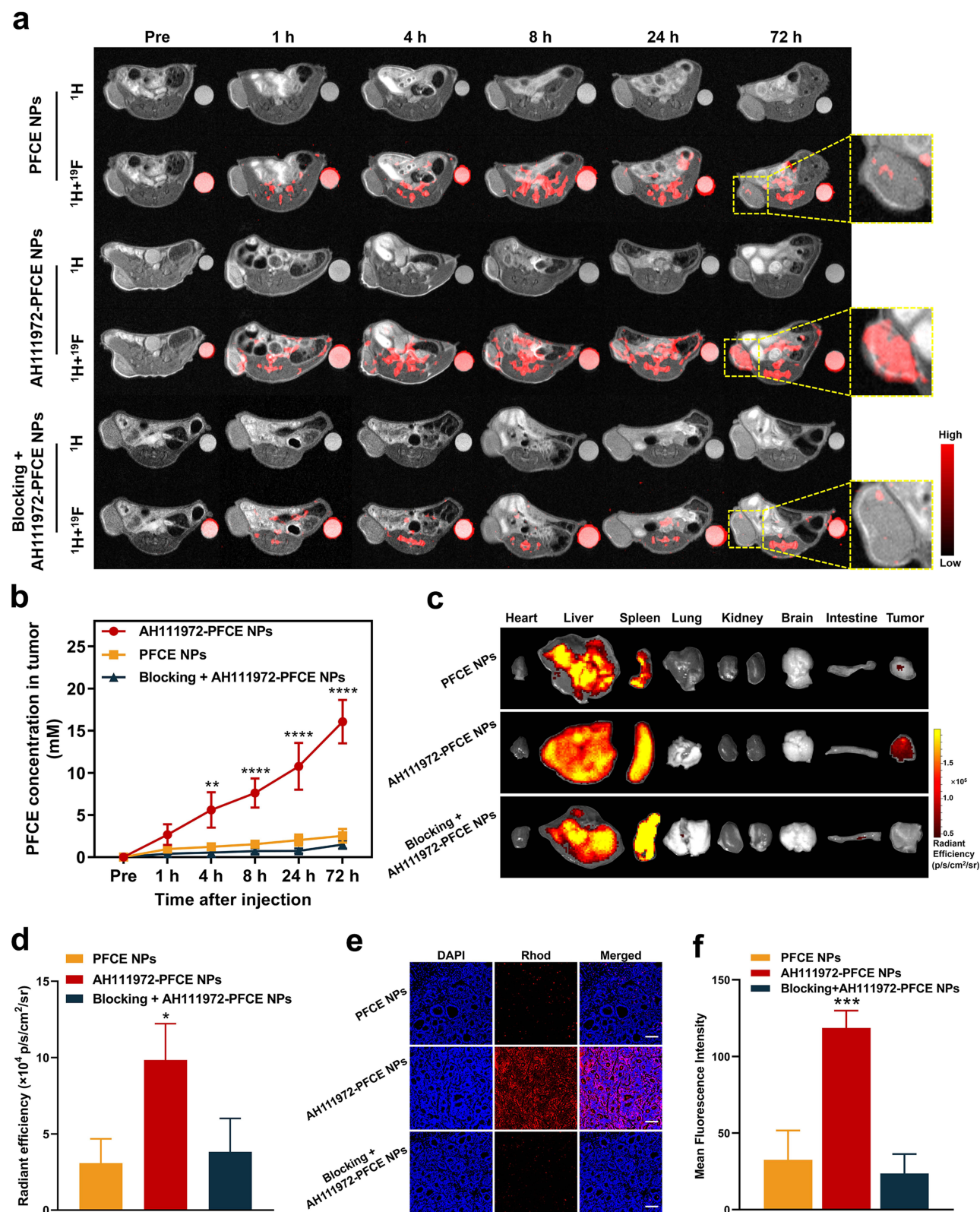


**Figure 4** Validation of c-Met specificity of AH111972-PFCE NPs in vivo. (a)  $^1\text{H}$  MR and colocalized  $^{19}\text{F}$  MR images of the subcutaneous tumor murine model in AH111972-PFCE NPs, PFCE NPs and blocking groups ( $n = 3/\text{group}$ ). For each mouse, 300  $\mu\text{L}$  of AH111972-PFCE NPs or PFCE NPs were injected intravenously via the tail vein. A solution of AH111972-PFCE in an EP tube was used as an internal reference. (b) Quantitative analysis of PFCE concentration in the subcutaneous tumor before and after injection. (c) Ex vivo near infrared fluorescence (NIRF) images of tumor and major organs derived from mice in each group. (d) Quantifications of rhodamine-emitted signal in tumors expressed as radiant efficiency. (e) Confocal laser scanning microscopy images of SW948 dissected tumor tissue in each group after the last MRI; Scale bar is 100  $\mu\text{m}$ . (f) Quantitative analysis of mean fluorescence intensity in SW948 dissected tumor tissue in each group after the last MRI. Data were expressed as mean  $\pm$  SD, \* $p < 0.05$ , \*\* $p < 0.01$ , \*\*\* $p < 0.001$ , \*\*\*\* $p < 0.0001$ .

PFCE NPs manifested excellent tumor permeability, which could be important for therapeutic applications and may be conducive to monitoring c-Met expression changes during progression and treatment.

### Small or Ill-Defined Colorectal Liver Metastases Precise Detection

We further evaluated the potential of AH111972-PFCE NPs in precise detection for liver metastases by  $^{19}\text{F}$  MRI. Mice with SW948 liver metastases were imaged after intravenously injecting AH111972-PFCE NPs and the non-targeting PFCE NPs used as a control.  $^{19}\text{F}$  MRI results of PFCE NPs group showed that the metastases were hardly be detected from the background uptake of normal liver, while multiple metastatic lesions could be clearly identified after injection of AH111972-PFCE NPs (Figure 5a). The difference of PFCE concentration at metastatic lesions between PFCE NPs and

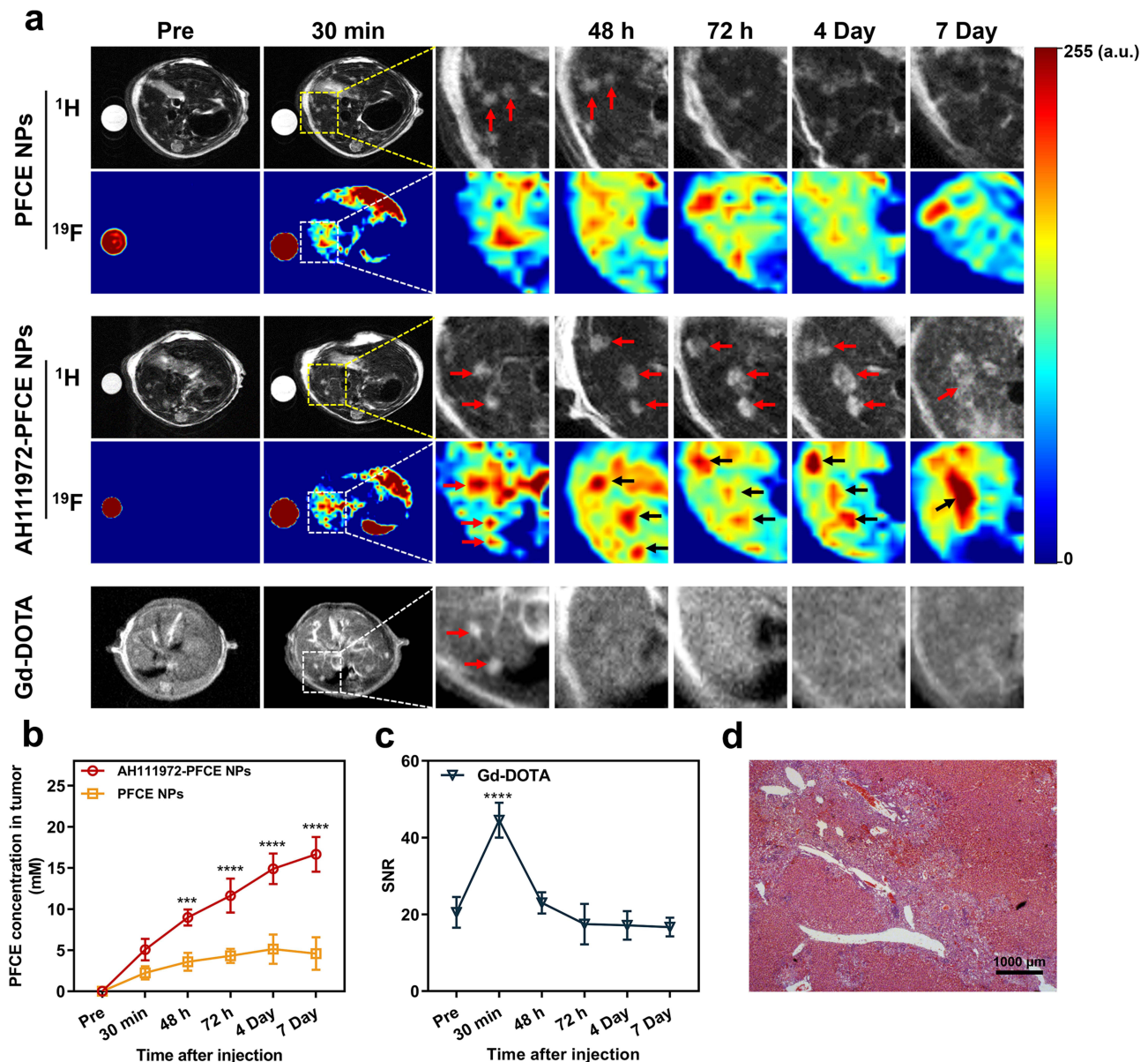


**Figure 5** Precise detection and long tumor retention of AH111972-PFCE NPs for colorectal liver metastases. (a)  $^1\text{H}$  MR and colocalized  $^{19}\text{F}$  MR images of the liver metastases murine model in AH111972-PFCE NPs and PFCE NPs groups as well as  $^1\text{H}$  MR images of the liver metastases murine model in Gd-DOTA group ( $n = 3/\text{group}$ ), red or black arrows indicate the metastases sites. For each mouse, 100  $\mu\text{L}$  of AH111972-PFCE NPs or PFCE NPs or 4  $\mu\text{L}$  of Gd-DOTA were injected intravenously via the tail vein. (b) Quantitative analysis of PFCE concentration of liver metastases in mice before and after the administration of c-Met-targeting and non-targeting PFCE nanoparticles. (c) Quantitative analysis of SNR of liver metastases in mice before and after Gd-DOTA injection. (d) H&E staining of liver with metastases in murine model with AH111972-PFCE NPs administration; Scale bar is 1000  $\mu\text{m}$ . Data were expressed as mean  $\pm$  SD, \*\*\* $p < 0.001$ , \*\*\*\* $p < 0.0001$ .



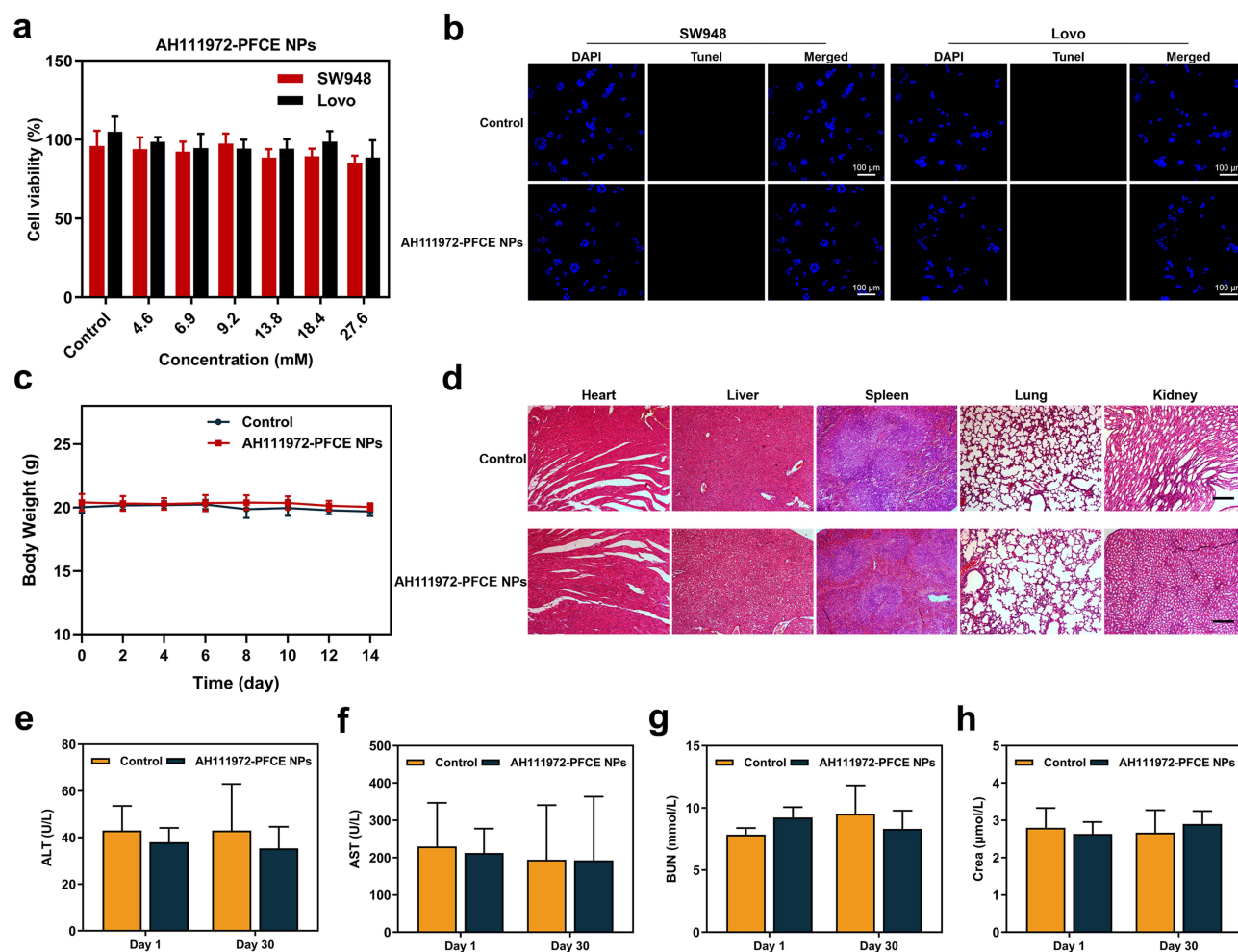


**Figure 6** Toxicity study of AH111972-PFCE NPs. (a) Viability of SW948 and Lovo cells after incubation with different concentrations of AH111972-PFCE NPs for 24 h. (b) Apoptosis in SW948 and Lovo cells was determined by TUNEL staining after incubation with AH111972-PFCE NPs for 24 h; Scale bar is 100 μm. (c) Body weight of mice in both groups within 14 days. (d) H&E staining of major organs (heart, liver, spleen, lung and kidney) in both groups 30 days after injection; Scale bar is 100 μm. (e–h) Indicators of liver and kidney function of mice intravenously injected with AH111972-PFCE NPs: (e) alanine aminotransferase (ALT), (f) aspartate aminotransferase (AST), (g) blood urea nitrogen (BUN) and (h) creatinine (Crea). The results are the average of three replicates ± standard deviation.

AH111972-PFCE NPs group was also compared and analyzed. The PFCE concentration of metastatic lesions increased gradually with time in mice after injection of AH111972-PFCE NPs. However, there was no remarkable change at the metastatic sites in the PFCE NPs group at all time points (Figure 5b). More importantly, for some smaller liver metastatic tumors missing by  $^1\text{H}$  MRI, the high  $^{19}\text{F}$  signal could be observed at 30 min post injection of AH111972-PFCE NPs and in the following 48 h to 7 d could dynamically monitor the process of the lesions from small to large and finally fused with others. In addition to the difficulty in detecting small lesions, the  $^1\text{H}$  MRI was also found too difficult to determine the ill-defined lesions from fusion metastases on the 7th day. By contrast, the fused metastases were obviously distinguished from the surrounding liver, and the outline was clear in c-Met-targeting  $^{19}\text{F}$  MRI (Figure 5a). The metastatic lesions identified by  $^{19}\text{F}$  MRI in AH111972-PFCE NPs group, were further confirmed by H&E staining (Figure 5d). These results demonstrated that  $^{19}\text{F}$  MRI with AH111972-PFCE NPs could precisely detect small or ill-defined colorectal liver metastases.

Although surgical resection remains the cornerstone treatment modality with the best chance for long-term survival, non-operative treatment is the optimal solution for most patients with CLMs.<sup>27,28</sup> Therefore, it is important to the evaluation of therapeutic efficacy by imaging monitoring of tumor during treatment. We also compared the long-term tumor retention capacity between AH111972-PFCE NPs and gadoterate meglumine (Gd-DOTA), a clinically used  $^1\text{H}$  MRI contrast agent. The results showed that the metastases became extraordinarily bright at 30 min post Gd-



DOTA injection but could hardly be distinguished from surrounding liver regions at subsequent time points. The time plot of liver metastases signal-to-noise ratio (SNR) change after Gd-DOTA injection showed that metastatic lesions SNR increased remarkably at 30 min post injection but reduced dramatically 48 h post injection (Figure 5c). On the contrary, the high  $^{19}\text{F}$  signal intensity of metastatic lesions in AH111972-PFCE NPs group could be maintained at a very high level for at least 7 days (Figure 5b). The long tumor retention may as a result of the binding of the peptide to cancer cells, a unique property of PFCE, and the appropriate size of the NPs ( $< 200$  nm). Unique features of PFCE, such as the insolubility in water and fat, and single resonance confer upon PFCE long in vivo retention times.<sup>29,30</sup> Since the tumor vascular gap is between 100 and 800 nm in size, particles smaller than 200 nm can pass through the gap more efficiently.<sup>31,32</sup> Long-term tumor retention of AH111972-PFCE NPs is conducive to the implementation of continuous therapeutic efficacy monitoring. Additionally, unlike traditional contrast agents, AH111972-PFCE NPs do not require repeated injections, reducing the occurrence of adverse reactions. Combined with robust c-Met targeting ability, this nanoplatform will contribute to increasing therapeutic agent accumulation in targeting sites as a novel carrier, laying a foundation for CLMs diagnosis and treatment integration.

## Toxicity Study of AH111972-PFCE NPs

In addition to the lack of targeting ability and short half-life, the possibility of NSF caused by the long-term accumulation of Gd and Gd brain deposition has raised concerns about the use of Gd-based contrast agents.<sup>33–35</sup> The results of the MTT assay showed that AH111972-PFCE NPs have no effect on cell viability in the 4.6 to 27.6 mM concentration range after 24 h of incubation (Figure 6a). The TUNEL assay showed that AH111972-PFCE NPs could not induce apoptosis of cancer cells, further proving their safety (Figures 6b and S4, Supporting Information). Moreover, the body weight of mice injected with AH111972-PFCE NPs had no remarkable changes in 14 days compared with the control group (Figure 6c). It was reported that the PFC NPs administered intravenously are mainly cleared from the mononuclear phagocyte system (MPS), such as the liver, spleen, along with bone marrow,<sup>36</sup> we also examined the effect of the AH111972-PFCE NPs on major organs, including the heart, liver, kidney, lung, and spleen, by H&E staining. Figure 6d shows no obvious sign of organ damage. The ALT, AST, BUN and Crea levels in mice injected with AH111972-PFCE NPs were comparable with control mice (Figure 6e–h). The WBC, RBC, and PLT levels in mice treated with AH111972-PFCE NPs showed no noticeable difference compared to the control group (Figure S5, Supporting Information). These results strongly confirm the safety of AH111972-PFCE NPs for diagnosis.

## Discussion

In this study, for the first time, we attached a c-Met-targeting cyclic peptide, AH111972, to the surface of PFCE NPs, offering new prospects for  $^{19}\text{F}$  MR molecular imaging in the precise diagnosis of CLMs. As shown from our results, due to the low sensitivity, small or fused metastases were either missed or ill-defined in  $^1\text{H}$  MRI. However, they were clearly identified in c-Met targeting  $^{19}\text{F}$  MRI. The c-Met-targeting nanoparticles, AH111972-PFCE NPs, could accumulate in tumor tissues via receptor-mediated internalization,<sup>37</sup> whereas the non-targeted nanoparticles concentration of tumor site remains relatively low because of the lack of cellular uptake. In the in vitro assay, the AH111972-PFCE NPs showed higher uptake by c-Met-overexpressing SW948 cancer cells than the non-targeted PFCE NPs evident in the competitive experiments. The robust tumor-targeting capability of the AH111972-PFCE NPs could be attributed to several factors. First, the 26-amino acid cyclic peptide AH111972 has a high affinity for c-Met. Second, the size of the AH111972-PFCE NPs contributes to increasing the ligand-receptor interaction per particle. Third, the NPs have long-term circulation allowing for increased tumor-targeting capability.<sup>24,25</sup> Finally, the negative surface charge of AH111972-PFCE NPs increases their stability in the serum-free culture medium and subsequently their affinity for the cell membrane.<sup>26</sup> Consistent with the in vitro cell uptake results, the results of in vivo  $^{19}\text{F}$  MRI also indicated that AH111972-PFCE NPs could targeting tumor sites effectively. Moreover, AH111972-PFCE NPs manifested excellent tumor permeability, which could be important for therapeutic applications and may be conducive to monitoring c-Met expression changes during progression and treatment.

Although surgical resection remains the cornerstone treatment modality with the best chance for long-term survival, non-operative treatment is the optimal solution for most patients with CLMs.<sup>27,28</sup> Therefore, it is important to the evaluation of therapeutic efficacy by imaging monitoring of tumor during treatment. As evident from our results, in the

$^1\text{H}$  MRI of liver metastases in mice injected with the clinical contrast agent, Gd-DOTA, the enhancement of tumor regions was negligible after 30 min. By contrast, aside from rapid tumor targeting (at 30th min), AH111972-PFCE NPs exhibited long tumor retention for at least 7 days, and the CLMs always be distinguished clearly during this period. Such characteristic of AH111972-PFCE NPs is conducive to the implementation of continuous therapeutic efficacy monitoring. Additionally, unlike traditional contrast agents, AH111972-PFCE NPs do not require repeated injections, reducing the occurrence of adverse reactions. Long-term tumor retention combined with robust c-Met targeting ability, this nanoplatform will contribute to increasing therapeutic agent accumulation in targeting sites as a novel carrier, laying a foundation for CLMs diagnosis and treatment integration. The long tumor retention may as a result of the binding of the peptide to cancer cells, a unique property of PFCE, and the appropriate size of the NPs ( $< 200$  nm). Unique features of PFCE, such as the insolubility in water and fat, and single resonance confer upon PFCE long in vivo retention times.<sup>29,30</sup> Since the tumor vascular gap is between 100 and 800 nm in size, particles smaller than 200 nm can pass through the gap more efficiently.<sup>31,32</sup>

In addition to the lack of targeting ability and short half-life, the possibility of NSF caused by the long-term accumulation of Gd and Gd brain deposition has raised concerns about the use of Gd-based contrast agents.<sup>33–35</sup> PFCs with stable chemical properties, good biocompatibility, and capability of carrying oxygen have been used as blood substitutes in the medical field.<sup>38–40</sup> It was reported that the PFC NPs administered intravenously are mainly cleared from the mononuclear phagocyte system (MPS), such as the liver, spleen, along with bone marrow,<sup>36</sup> also supported by our results from the in vivo MRI and ex vivo biodistribution study. Although AH111972-PFCE NPs were removed from MPS, the H&E staining of major organs, especially the liver and spleen, did not exhibit apparent damage in the experimental group compared with the control group. Additionally, biochemical parameters together with routine blood indices in the in vivo model remained at levels comparable to those in the control group. These results strongly confirm the safety of AH111972-PFCE NPs for diagnosis.

## Conclusion

We have synthesized c-Met-targeting AH111972-PFCE NPs for the in vivo detection of small and ill-defined CLMs by  $^{19}\text{F}$  MRI. The nanoparticles showed applicable structural characteristics, superior  $^{19}\text{F}$  NMR and MRI properties. The excellent c-Met specificity and long-term tumor retention ability of AH111972-PFCE NPs evidenced that the PFCE NPs conjugated with c-Met-targeting peptides are eminent candidates for the precise detection of small and ill-defined CLMs by  $^{19}\text{F}$  MRI. Moreover, considering the application of some kinds of PFC in the clinic and the outstanding biosafety of the peptide-functionalized NPs, AH111972-PFCE NPs are expected to replace existing MR contrast agents and could be a nanoplatform applicable to precise diagnosis, therapeutic efficacy monitoring and drug delivery for patients with CLMs.

## Acknowledgments

Daoshuang Li and Jie Yang contributed equally to this work. This work was supported by the National Natural Science Foundation of China (81627901 and 82102101), Natural Science Foundation of Heilongjiang Province (Grant No. JQ2020H002), HMU Marshal Initiative Funding (HMUMIF-21003), the Tou-Yan Innovation Team Program of the Heilongjiang Province (2019-15), and Heilongjiang Provincial Key Laboratory of Molecular Imaging foundation.

## Disclosure

The authors report no conflicts of interest in this work.

## References

1. Hess KR, Varadhachary GR, Taylor SH, et al. Metastatic patterns in adenocarcinoma. *Cancer*. 2006;106(7):1624–1633. doi:10.1002/cncr.21778
2. Manfredi S, Lepage C, Hatem C, Coatmeur O, Faivre J, Bouvier AM. Epidemiology and management of liver metastases from colorectal cancer. *Ann Surg*. 2006;244(2):254–259. doi:10.1097/01.sla.0000217629.94941.cf
3. Bae MS, Shin SU, Ryu HS, et al. Pretreatment MR imaging features of triple-negative breast cancer: association with response to neoadjuvant chemotherapy and recurrence-free survival. *Radiology*. 2016;281(2):392–400. doi:10.1148/radiol.2016152331

4. Stark DD, Moss AA, Goldberg HI. Nuclear magnetic resonance of the liver, spleen, and pancreas. *Cardiovasc Intervent Radiol*. 1986;8(5–6):329–341. doi:10.1007/BF02552370
5. Zhou Z, Qutaish M, Han Z, et al. MRI detection of breast cancer micrometastases with a fibronectin-targeting contrast agent. *Nat Commun*. 2015;6:7984. doi:10.1038/ncomms8984
6. Al-Maghribi J, Emam E, Gomaa W, et al. c-MET immunostaining in colorectal carcinoma is associated with local disease recurrence. *BMC Cancer*. 2015;15:676. doi:10.1186/s12885-015-1662-6
7. Yao JF, Li XJ, Yan LK, et al. Role of HGF/c-Met in the treatment of colorectal cancer with liver metastasis. *J Biochem Mol Toxicol*. 2019;33(6):e22316. doi:10.1002/jbt.22316
8. Wang S, Ma H, Yan Y, et al. cMET promotes metastasis and epithelial-mesenchymal transition in colorectal carcinoma by repressing RKIP. *J Cell Physiol*. 2021;236(5):3963–3978. doi:10.1002/jcp.30142
9. Song EK, Tai WM, Messersmith WA, et al. Potent antitumor activity of cabozantinib, a c-MET and VEGFR2 inhibitor, in a colorectal cancer patient-derived tumor explant model. *Int J Cancer*. 2015;136(8):1967–1975. doi:10.1002/ijc.29225
10. Lev A, Deihimi S, Shagisultanova E, et al. Preclinical rationale for combination of crizotinib with mitomycin C for the treatment of advanced colorectal cancer. *Cancer Biol Ther*. 2017;18(9):694–704. doi:10.1080/15384047.2017.1364323
11. Wolf J, Seto T, Han JY, et al. Capmatinib in MET exon 14-mutated or MET-amplified non-small-cell lung cancer. *N Engl J Med*. 2020;383(10):944–957. doi:10.1056/NEJMoa2002787
12. Schuler M, Berardi R, Lim WT, et al. Molecular correlates of response to capmatinib in advanced non-small-cell lung cancer: clinical and biomarker results from a Phase I trial. *Ann Oncol*. 2020;31(6):789–797. doi:10.1016/j.annonc.2020.03.293
13. Bree RL, Schwab RE, Glazer GM, Fink-Bennett D. The varied appearances of hepatic cavernous hemangiomas with sonography, computed tomography, magnetic resonance imaging and scintigraphy. *Radiographics*. 1987;7(6):1153–1175. doi:10.1148/radiographics.7.6.3321218
14. Villaraza AJ, Bumb A, Brechbiel MW. Macromolecules, dendrimers, and nanomaterials in magnetic resonance imaging: the interplay between size, function, and pharmacokinetics. *Chem Rev*. 2010;110(5):2921–2959. doi:10.1021/cr900232t
15. Shin TH, Choi Y, Kim S, Cheon J. Recent advances in magnetic nanoparticle-based multi-modal imaging. *Chem Soc Rev*. 2015;44(14):4501–4516. doi:10.1039/C4CS00345D
16. Major JL, Meade TJ. Bioresponsive, cell-penetrating, and multimeric MR contrast agents. *Acc Chem Res*. 2009;42(7):893–903. doi:10.1021/ar800245h
17. Kobayashi H, Kawamoto S, Saga T, et al. Novel liver macromolecular MR contrast agent with a polypropylenimine diaminobutyl dendrimer core: comparison to the vascular MR contrast agent with the polyamidoamine dendrimer core. *Magn Reson Med*. 2001;46(4):795–802. doi:10.1002/mrm.1259
18. DeVience SJ, Pham LM, Lovchinsky I, et al. Nanoscale NMR spectroscopy and imaging of multiple nuclear species. *Nat Nanotechnol*. 2015;10(2):129–134. doi:10.1038/nnano.2014.313
19. Tirota I, Dichiarante V, Pigliacelli C, et al. (19)F magnetic resonance imaging (MRI): from design of materials to clinical applications. *Chem Rev*. 2015;115(2):1106–1129. doi:10.1021/cr500286d
20. Chen J, Lanza GM, Wickline SA. Quantitative magnetic resonance fluorine imaging: today and tomorrow. *Wiley Interdiscip Rev Nanomed Nanobiotechnol*. 2010;2(4):431–440. doi:10.1002/wnan.87
21. Li Y, Cui J, Li C, et al. (19)F MRI nanotheranostics for cancer management: progress and prospects. *ChemMedChem*. 2022;17(4):e202100701. doi:10.1002/cmdc.202100701
22. Jacoby C, Temme S, Mayenfels F, et al. Probing different perfluorocarbons for in vivo inflammation imaging by 19F MRI: image reconstruction, biological half-lives and sensitivity. *NMR Biomed*. 2014;27(3):261–271. doi:10.1002/nbm.3059
23. Wu L, Wen X, Wang X, et al. Local intratracheal delivery of perfluorocarbon nanoparticles to lung cancer demonstrated with magnetic resonance multimodal imaging. *Theranostics*. 2018;8(2):563–574. doi:10.7150/thno.21466
24. Jain RK, Stylianopoulos T. Delivering nanomedicine to solid tumors. *Nat Rev Clin Oncol*. 2010;7(11):653–664. doi:10.1038/nrclinonc.2010.139
25. Albanese A, Tang PS, Chan WC. The effect of nanoparticle size, shape, and surface chemistry on biological systems. *Annu Rev Biomed Eng*. 2012;14:1–16. doi:10.1146/annurev-bioeng-071811-150124
26. Kolosnjaj-Tabi J, Wilhelm C, Clément O, Gazeau F. Cell labeling with magnetic nanoparticles: opportunity for magnetic cell imaging and cell manipulation. *J Nanobiotechnol*. 2013;11(Suppl1):S7. doi:10.1186/1477-3155-11-S1-S7
27. Alberts SR, Poston GJ. Treatment advances in liver-limited metastatic colorectal cancer. *Clin Colorectal Cancer*. 2011;10(4):258–265. doi:10.1016/j.clcc.2011.06.008
28. Gillams A, Goldberg N, Ahmed M, et al. Thermal ablation of colorectal liver metastases: a position paper by an international panel of ablation experts, The Interventional Oncology Sans Frontières meeting 2013. *Eur Radiol*. 2015;25(12):3438–3454. doi:10.1007/s00330-015-3779-z
29. Staal AHJ, Becker K, Tagit O, et al. In vivo clearance of (19)F MRI imaging nanocarriers is strongly influenced by nanoparticle ultrastructure. *Biomaterials*. 2020;261:120307. doi:10.1016/j.biomaterials.2020.120307
30. Dobrovolskaia MA, Aggarwal P, Hall JB, McNeil SE. Preclinical studies to understand nanoparticle interaction with the immune system and its potential effects on nanoparticle biodistribution. *Mol Pharm*. 2008;5(4):487–495. doi:10.1021/mp800032f
31. Sun T, Zhang YS, Pang B, Hyun DC, Yang M, Xia Y. Engineered nanoparticles for drug delivery in cancer therapy. *Angew Chem Int Ed Engl*. 2014;53(46):12320–12364. doi:10.1002/anie.201403036
32. Haley B, Frenkel E. Nanoparticles for drug delivery in cancer treatment. *Urol Oncol*. 2008;26(1):57–64. doi:10.1016/j.urolonc.2007.03.015
33. Marckmann P, Skov L, Rossen K, et al. Nephrogenic systemic fibrosis: suspected causative role of gadodiamide used for contrast-enhanced magnetic resonance imaging. *J Am Soc Nephrol*. 2006;17(9):2359–2362. doi:10.1681/ASN.2006060601
34. Kanda T, Fukusato T, Matsuda M, et al. Gadolinium-based contrast agent accumulates in the brain even in subjects without severe renal dysfunction: evaluation of autopsy brain specimens with inductively coupled plasma mass spectroscopy. *Radiology*. 2015;276(1):228–232. doi:10.1148/radiol.2015142690
35. Adin ME, Kleinberg L, Vaidya D, Zan E, Mirbagheri S, Yousem DM. Hyperintense dentate nuclei on T1-weighted MRI: relation to repeat gadolinium administration. *AJNR Am J Neuroradiol*. 2015;36(10):1859–1865. doi:10.3174/ajnr.A4378
36. Giraudeau C, Djemai B, Ghaly MA, et al. High sensitivity 19F MRI of a perfluorooctyl bromide emulsion: application to a dynamic biodistribution study and oxygen tension mapping in the mouse liver and spleen. *NMR Biomed*. 2012;25(4):654–660. doi:10.1002/nbm.1781

37. Sukumar UK, Bhushan B, Dubey P, Matai I, Packirisamy G, Packirisamy G. Emerging applications of nanoparticles for lung cancer diagnosis and therapy. *Int Nano Letters*. 2013;3(1):1–17. doi:10.1186/2228-5326-3-45
38. Hong F, Shastri K, Logue G, Spaulding M. Complement activation by artificial blood substitute Fluosol: in vitro and in vivo studies. *Transfusion*. 1991;31(7):642–647. doi:10.1046/j.1537-2995.1991.31791368343.x
39. Lowe K. Perfluorinated blood substitutes and artificial oxygen carriers. *Blood Rev*. 1999;13(3):171–184. doi:10.1054/blre.1999.0113
40. Spiess BD. Perfluorocarbon emulsions as a promising technology: a review of tissue and vascular gas dynamics. *J Appl Physiol*. 2009;106(4):1444–1452. doi:10.1152/jappphysiol.90995.2008

## International Journal of Nanomedicine

Dovepress

### Publish your work in this journal

The International Journal of Nanomedicine is an international, peer-reviewed journal focusing on the application of nanotechnology in diagnostics, therapeutics, and drug delivery systems throughout the biomedical field. This journal is indexed on PubMed Central, MedLine, CAS, SciSearch®, Current Contents®/Clinical Medicine, Journal Citation Reports/Science Edition, EMBase, Scopus and the Elsevier Bibliographic databases. The manuscript management system is completely online and includes a very quick and fair peer-review system, which is all easy to use. Visit <http://www.dovepress.com/testimonials.php> to read real quotes from published authors.

Submit your manuscript here: <https://www.dovepress.com/international-journal-of-nanomedicine-journal>